



Hydrodynamic forces on emergent cylinders in non-uniform flow

Tatsuhiko Uchida¹ · Toshiki Ato² · Daisuke Kobayashi³ · Mahmoud F. Maghrebi⁴ · Yoshihisa Kawahara⁵

Received: 7 October 2021 / Accepted: 14 September 2022
© The Author(s) 2022

Abstract

The main objective of conducting numerical simulations of flows in rivers with vegetation is to investigate the complex flow dynamics involved in non-equilibrium conditions. In such cases, it is inappropriate to apply the drag coefficient C_D , which is typically derived based on uniform flows involving groups of infinitely long cylinders. This paper presents a method for evaluating the drag forces acting on emergent obstacles for non-uniform open-channel flows. This method is devised based on two sets of experiments: on flows with small-diameter cylinders, focusing on the water surface profiles through the group; and on flows with large-diameter cylinders, focusing on the local pressure distribution and local water surface profile around a target cylinder. In addition to the conventional drag force expression that includes C_D , two new terms are proposed to account for the effects of water surface variation and pressure gradient in non-uniform open-channel flow on the drag. The first of these terms, which introduces the use of the Froude number to account for the effect of water surface variation, is derived theoretically and evaluated against past and present experimental results under uniform-flow conditions. On the other hand, the second of these terms, which includes the representative length of the separation zone to evaluate the effect of pressure gradient, is confirmed to be a necessity through numerical calculation of the longitudinal water surface profile in emergent cylinders. The incorporation of these two terms using a simple unified expression can help improve the accuracy of numerical simulations for practical problems of flows with emergent obstacles.

Highlights

- (1) Conventional drag-force terms are shown to be insufficient for calculations of water flows with emergent obstacles.
- (2) The effect of water surface variation on the drag force is derived theoretically as a function of the Froude number.
- (3) For accelerating flows, additional drag forces are revealed by local pressure distribution and water surface profiles.

✉ Tatsuhiko Uchida
utida@hiroshima-u.ac.jp

Extended author information available on the last page of the article

Keywords Accelerating flow · Drag coefficient · Emergent cylinder array · Pressure gradient · Water surface profile

1 Introduction

The effects of vegetation on water flow, turbulence, and sediment transport have attracted considerable interest from researchers in a variety of fields [1–4]. For example, it has been demonstrated that the characteristics of canopy flows should be clearly determined to properly understand the behaviors of wind flows involving forest canopies [5, 6] and groups of buildings in urban areas [7], as well as the behaviors of water flows involving coral reefs [8] and in gravel-bed rivers with boulders [9–11]. It is also important to know the resistance characteristics of a group of cylinders in fluid flow because of the occurrence of this structure in a number of applications of fluid dynamics, such as heat exchangers, where arrays of cylinders are a common configuration [12].

Generally, in flow calculations, multiscale obstacles are divided based on two characteristic scales: large-scale topography, which can be resolved using a computational mesh explicitly as a boundary shape; and small-scale topography, which is evaluated using sub-scale models [9, 11]. In a number of studies, numerical simulations of flows through vegetation have been conducted using fine meshes to resolve the effects of obstacles [7, 13]; in others, the effects of vegetation have been modeled using temporal-spatial averaging of the governing equations [3, 5, 6, 8, 14–18]. Based on the complexity of vegetation conditions in rivers, the second aforementioned approach is considered to be suitable for practical applications [18–20]. When averaged over space in Reynolds-averaged Navier–Stokes equations for local flows, in addition to the dispersion term due to sub-average-scale flows, the fluid force terms appear in conjunction with Gauss’ divergence theorem in the momentum equation integrating the local pressure distribution and shear stress acting on the objects [6, 15]. The problem, as with the closure problem for turbulence, is how to represent the hydrodynamic force terms induced by sub-average-scale flows around the boundaries and distinguish them from the average-scale flow [21]. The drag-force terms in the momentum equations are evaluated using drag coefficients, which determine the accuracy of the models [22]. The drag coefficients also appear in equations for evaluating the turbulence intensity and dispersion coefficients of passive particles in water flows [3, 14, 17, 23, 24].

Meanwhile, several studies have contributed to determining the drag induced by vegetation [25–29]. However, although actual vegetation tends to be irregularly shaped and flexible [18], circular cylinders have been employed to model rigid vegetation in calculations regarding the characteristics of canopy flow. The drag coefficient C_D of a circular cylinder in a free-stream flow (defined as a uniform flow that lacks a free surface, and typically distinguished from a uniform open-channel flow) is known to be a function of the Reynolds number $\mathcal{R} = Vd/\nu$ (V , free-stream velocity; d , cylinder diameter; ν , kinematic viscosity); the same is true for a sphere among several representative immersed bodies [30–32]. The variation in the drag coefficient of an array of cylinders depends on the space between the cylinders and the density of the array. Several researchers have contributed to correlating drag coefficients of cylinder arrays with well-established relationships between the drag-force coefficient and Reynolds number for a single cylinder. For example, Koch and Ladd [25] and Tanino and Nepf [26] applied the equation proposed by Ergun [33], which was devised for pressure drops in packed columns, to the drag coefficient and Reynolds

number function. Kothyari et al. [34] proposed a relationship between the drag coefficient and Reynolds number for subcritical flows as a positive logarithmic function of the density, showing that the drag coefficient increases rapidly for low density values. Cheng [35] proposed a formula for the drag coefficient of a cylinder array by expanding the relationship for an isolated cylinder based on the concept of a pseudo-fluid model [36] and validated the formula against several drag-force coefficient datasets.

On the other hand, in contrast to most canopy flows, open-channel flows, such as in rivers, involve the Froude number $\mathcal{F} = V/(gh)^{0.5}$ (g , gravity; h , water depth), an important dimensionless parameter that influences the drag coefficient, especially for emergent obstacles in shallow-water flows. In fact, the drag coefficients of hydraulic structures are related to the Froude number [31]. However, only a few studies have investigated the effect of the Froude number on the drag coefficients of emergent cylinders in open-channel flows. Furthermore, Kothyari et al. [34] indicated that, whereas the drag coefficient is not substantially influenced by the Froude number in subcritical flows, the coefficient decreases with respect to the Froude number in supercritical flows. The results of a study by Huai et al. [37], in which a large-eddy numerical simulation model was used in conjunction with three identical-density conditions, showed that C_D largely decreases as \mathcal{F} increases. It is significant that C_D is smaller in supercritical flows than in subcritical flows; however, the underlying mechanism for this distinction has not yet been elucidated.

Most previous studies on the evaluation of drag forces and flow resistance were conducted based on uniform open-channel flows. However, to fulfill the objective of applying drag-force coefficients to numerical simulations of flows in natural rivers [19, 20], a method for evaluating the effects of non-equilibrium flow in average scales on the resistance must be developed. For example, Busari and Li [38] investigated the interference effects of finite-length vegetation in gradually varied flows, whereas Uchida et al. [11] proposed a dynamic rough-wall law to account for the effect of non-equilibrium flow near a bed with submerged boulders on the flow resistance. However, despite these efforts, there has been insufficient research on methods for evaluating the direct effects of non-equilibrium open-channel flows on the drag force.

To take into account the resistance of vegetation in rivers, it is necessary to elucidate the effects of variations in the water surfaces around obstacles. For non-equilibrium flows with pressure gradients in an average scale, because the separation regions behind the obstacles exhibit low flow velocities [12, 39, 40], pressures acting on the backs of the obstacles are inferred to be affected by the pressure downstream in the scale of the separation length.

The objective of this study is to develop a method for evaluating the drag coefficient of emergent cylinders in an array in a non-uniform open-channel flow. The proposed method is to be designed for numerical simulations. In addition to the conventional drag-force expression, which includes the drag coefficient, this paper proposes two new terms for evaluating the effects of water surface variation in a local scale and pressure gradient in an average scale on the drag force for emergent cylinders. For the first term, a drag-coefficient equation is derived theoretically as a function of the Froude number. This equation is compared with drag coefficients from previous experiments and our laboratory experiment on uniform flows without the introduction of any calibration parameters. For the second term, the representative length of the separation zone is introduced to evaluate the effect of the pressure gradient in the average scale on the drag force in non-uniform open channel flows. The calculation of gradually varied flows with emergent cylinders reveals the necessity of the term to account for the effect of the pressure gradient on the drag forces in accelerating flows. The validity of the term is supported by the results of supplementary experiments that focus on the distribution of pressure on a cylinder in a group. Based on this pressure

distribution, the negative pressure gradient for accelerating flow decreases the pressure in the separation zone behind the cylinder. It is then demonstrated that several non-uniform water-surface profiles, including accelerating and decelerating flows, can be reproduced well using a simple unified expression incorporating these two terms.

2 Experimental setup

Two sets of experiments were conducted in this study. The first set of experiments investigated longitudinal water surface profiles using an experimental channel, in which several small-scale emergent cylinders were installed, and focused on developing a method for evaluating the resistance. To clarify the effects of water surface variation and pressure gradients on drag force, three types of flow behavior, i.e., uniform, accelerating, and decelerating flows, were examined. The second set of experiments involved a supplemental study that elucidated the mechanism of the hydrodynamic force and pressure distribution on emergent cylinders. This experiment was conducted to measure the local water surface variations around large-scale emergent cylinders and the distribution of pressure acting on a cylinder in the group.

The first set of experiments was conducted in a water-recirculating flume (length, 3.0 m; width B , 0.3 m) with varying channel slopes. The flows were adjusted to either uniform or non-uniform flow using a weir installed downstream. For this study, we regard uniform flow as that when the water surface gradients coincide with the channel gradient. The emergent cylinders were circular wooden dowels (diameter d , 10 mm; height, 20 cm). The Styrofoam floor of the flume was drilled, and the dowels were installed individually in longitudinal and lateral intervals Δx and Δy , respectively, of 0.0344 m in a staggered array from the downstream end of the channel (Fig. 1) to

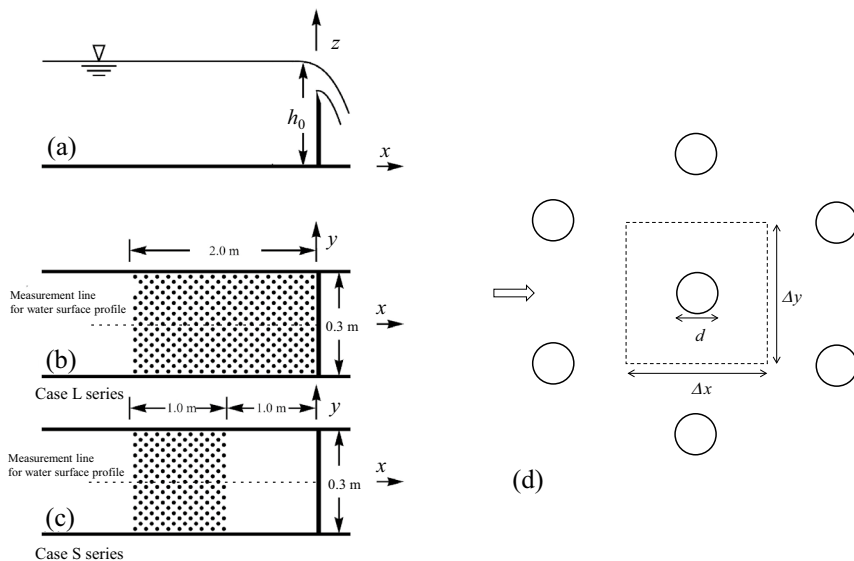


Fig. 1 Experimental setup of flume and cylinders: **a** side view (cylinders omitted); **b**, **c** plan views; **d** magnified plan view

maximize the flow resistance. The density of cylinders per unit area, λ , is defined as $\lambda = N\pi d^2/4$, where N is the number of cylinders per unit area (present experimental conditions: $N = 1/(\Delta x \Delta y)$), and d is the cylinder diameter. The density $\lambda = 0.067$ in this experiment is in the range of actual vegetation densities in the flood plains of Japan [41].

The experiments consisted of Case L and S series: In the Case L series (Fig. 1b), the cylinders cover the last 2.0 m of the flume, whereas in the Case S series (Fig. 1c), the cylinders cover only 1.0 m of the flume between the upstream and downstream ends. Flow depth was measured using a point gauge with a 0.1-mm vernier scale mounted on a carriage that could be moved along the flume rails. The water depth h was measured along the longitudinal axis on the centerline of the flume at intervals of 0.2 m. The resistance evaluation in this study is based on the results of this water surface profile measurement, i.e., the focus of this study is the modeling of phenomena that can affect the larger-scale analyses of one-dimensional measurement approaches, such as water surface profiles. On the other hand, the effects of the upstream and downstream ends of a cylinder group on the internal structure, such as on the velocity distribution and turbulence in two- or three-dimensional flow structures, are not included in this study. Investigations regarding these aspects of flow behavior will require further advancement of the results of this research. The volumetric discharge was measured using a triangular weir with a tank 0.8 m in length, 0.4 m in width, and 0.4 m in height. The average cross-sectional velocity (bulk velocity) U was defined using the mean depth h as $U = Q/(hB)$, where Q and B are the discharge and width of the flume, respectively.

There are several possible definitions of representative velocity for evaluating canopy drag, including bulk velocity U [16–18, 42, 43], pore velocity $U_p = U/(1 - \lambda)$ [18, 26, 34, 41], and constructed velocity $U_c = U/(1 - d/\Delta y)$ [44]. The undisturbed velocity, which is defined as a local velocity removing the target obstacle, is considered appropriate to evaluate a local pressure change by installing the target obstacle [45–47]. Because the local pressure change around the obstacle induces the hydrodynamic force, the representative velocities include the bulk, pore, and constructed velocities, which can be regarded as attempts to estimate the undisturbed velocity. However, the undisturbed velocity is affected by other cylinders and hydraulic conditions, and thus a proper method for the evaluation of the undisturbed velocity has not yet been established [47]. The definition of representative velocity is also relevant to discussions regarding the representative flow velocity for the Froude number, which is relevant to deriving the depth profile equation (see Eq. 8). In this study, the vegetation density was relatively low, and its effect was small [18]. Furthermore, as in many numerical calculations on flows involving vegetation [16, 17, 20], the bulk velocity was employed to focus on the effects of the water surface and pressure gradient on the drag coefficient. Nevertheless, there remain questions regarding the representative velocity for future studies to resolve.

Table 1 summarizes the bed slope and discharge conditions for the experiments on uniform, accelerating, and decelerating open-channel flows. For Cases L1–L6, the differences in the gradients between the water surface and bed, calculated using measurements obtained at 0.2-m intervals over 1.4 m, were less than 0.4×10^{-4} . Large values of \mathcal{R} were used to decrease the dependence of the drag coefficient on the Reynolds number [26–29, 34, 35, 48]. To distinguish the effects of the Froude number from those of the Reynolds number, a more detailed investigation will be necessary because the effect of the Reynolds number on the drag coefficient varies with cylinder conditions [25–29]. Thus, instead of analyzing a large amount of drag coefficient data, we examine the effects of the Froude number and water surface theoretically in the following section.

Table 1 Experimental conditions for staggered array of vertical, rigid circular cylinders

| Case ^a | Discharge Q (10^{-3} $\text{m}^3 \text{s}^{-1}$) | Bed slope (δ_0) | Flow behavior ^b | Flow depth ^c h_0 (m) | Reynolds number (R) | Froude number (F) | Drag coefficient (C_D) |
|-------------------|--|--------------------------|----------------------------|-----------------------------------|---|-----------------------------|----------------------------|
| L1 | 3.33 | 2.8×10^{-3} | UN | 0.164 | 6.7×10^2 | 0.05 | 1.17 |
| L2 | 2.07 | 2.8×10^{-3} | UN | 0.104 | 6.6×10^2 | 0.07 | 1.42 |
| L3 | 5.70 | 5.8×10^{-2} | UN | 0.059 | 3.2×10^3 | 0.41 | 1.27 |
| L4 | 6.55 | 5.8×10^{-2} | UN | 0.065 | 3.4×10^3 | 0.44 | 1.07 |
| L5 | 3.95 | 5.8×10^{-2} | UN | 0.039 | 3.3×10^3 | 0.53 | 1.15 |
| L6 | 1.73 | 5.8×10^{-2} | UN | 0.015 | 3.9×10^3 | 1.01 | 0.91 |
| L7 | 4.85 | 2.8×10^{-3} | AC | 0.052 | $1.6 \times 10^3 < \mathcal{R} < 3.1 \times 10^3$ | $0.17 < \mathcal{F} < 0.44$ | – |
| L8 | 2.06 | 2.8×10^{-3} | AC | 0.032 | $1.2 \times 10^3 < \mathcal{R} < 2.1 \times 10^3$ | $0.16 < \mathcal{F} < 0.38$ | – |
| L9 | 2.25 | 5.8×10^{-2} | DC | 0.060 | $1.2 \times 10^3 < \mathcal{R} < 4.1 \times 10^3$ | $0.16 < \mathcal{F} < 0.98$ | – |
| L10 | 3.67 | 5.8×10^{-2} | DC | 0.106 | $1.1 \times 10^3 < \mathcal{R} < 3.4 \times 10^3$ | $0.11 < \mathcal{F} < 0.59$ | – |
| S1 | 5.35 | 2.8×10^{-3} | AC | 0.101 | $1.5 \times 10^3 < \mathcal{R} < 1.6 \times 10^3$ | $0.14 < \mathcal{F} < 0.16$ | – |
| S2 | 5.35 | 2.8×10^{-3} | AC | 0.066 | $1.8 \times 10^3 < \mathcal{R} < 2.7 \times 10^3$ | $0.19 < \mathcal{F} < 0.35$ | – |

^aFirst letter (case series) identifies extent of vegetation zone: L long; S short

^bAC accelerating; DC decelerating; UN uniform

^cMeasured at location 0.1 m upstream of downstream gate

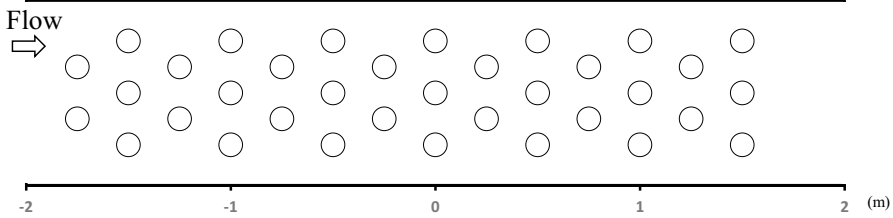


Fig. 2 Experimental setup with large-cylinder array for measuring pressure distribution around cylinders and local water surface profiles

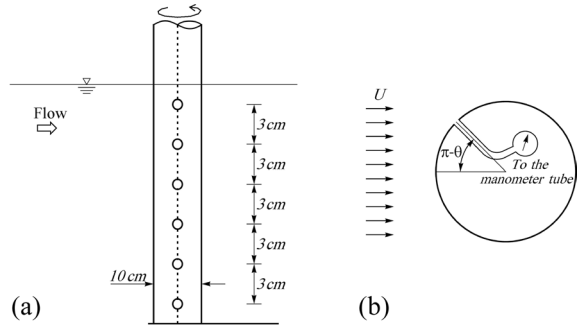
Table 2 Experimental conditions for pressure distribution on emergent cylinder

| Coefficient or parameter | Free stream (Rouse [30]) | Uniform flow | Accelerating flow |
|--------------------------|--------------------------|-------------------|---------------------------------------|
| h_p (m) ^a | – | 0.18 | 0.13 |
| R | 1.86×10^5 | 2.7×10^4 | 3.6×10^4 – 6.8×10^4 |
| F | – | 0.18 | 0.33–0.62 |
| C_{pmin} | –1.40 | –2.55 | –3.43 |
| C_{D0} | 1.29 | 1.79 | 2.68 |
| β_{Cp} | –0.24 | –0.40 | –0.51 |
| dh/dx | – | 0 | –0.02 |

^aWater depth on pressure-measurement cylinder

The second set of experiments, a supplementary study using larger-scale cylinders (diameter 0.1 m), was conducted in a channel of width 0.8 m and length 24 m to measure the local water surface around an emergent cylinder and the distribution of pressures acting on it. The channel slope was 1/200. The cylinders, 3.3 m in length, were installed in a staggered array with $\Delta x = 0.25$ m and $\Delta y = 0.225$ m, as shown in Fig. 2. The experiments included uniform-flow and acceleration conditions with a constant experimental discharge Q of $0.035 \text{ m}^3 \text{ s}^{-1}$. The experimental conditions are summarized in Table 2. In this set of experiments, the representative velocity for calculating the pressure coefficient and drag coefficient was measured using a MicroADV (SonTek) probe based on an undisturbed flow, i.e., without the cylinder of interest, to eliminate the effect of high velocities along the sidewalls, which were due to the small number of cylinders in the transverse direction (each row comprised only two or three cylinders, as shown in Fig. 2). The vertical distribution of pressures acting on the center cylinder of the group was also obtained. Figure 3 shows the pressure-measurement cylinder installed in the center of the group ($x=0$ in Fig. 2). This 10-cm-diameter cylinder, along the side of which six equidistant holes were drilled (3 cm apart), was used to measure the pressure at different water depths. The cylinder was equipped with 5-mm-diameter tubes, which were connected to manometer glass tubes with a diameter of 0.6 mm. The pressure p on the cylinder was measured at an arbitrary angle θ with respect to the flow using the manometers as the pressure-measurement cylinder was rotated. The measurements were performed at intervals of $\pi/18$. The accuracy of the pressure measurement using the manometers was estimated to be 0.2–0.3 mm based on averages over the vertical pressure points for each angle.

Fig. 3 Pressure-measurement cylinder with manometers



3 Equation of water surface profile for flow with cylinders

To determine the relationship between the water surface profiles and drag forces on the vegetation, we first consider the momentum equation in the streamwise direction for shallow-water flows (hydrostatic pressure and no vertical velocity distribution) in a wide rectangular channel:

$$\rho \left(\frac{\partial U}{\partial t} + U \frac{\partial U}{\partial x} \right) = \rho g S_0 - \rho g \frac{\partial h}{\partial x} - \frac{f_t}{h} \tag{1}$$

where f_t is the external force acting on the water column in a unit area, including the shear stress on the channel bed and drag forces on the vegetation. For a steady-flow condition, we have

$$q = Uh = \text{const.} \tag{2}$$

where q is the unit flow discharge. By substituting Eq. (2) into Eq. (1), we obtain

$$(1 - \mathcal{F}^2) \frac{dh}{dx} = S_0 - \frac{f_t}{\rho gh} \tag{3}$$

where $\mathcal{F}^2 = q^2 / gh^3$. For the case involving no cylinders, $f_t = \tau_0 = \rho g S_f$ (τ_0 , bed shear stress; S_f , friction slope); therefore, the well-known governing equation for gradually varied flows [30, 49] can be obtained. For flows with emergent-cylinder vegetation models, the total force f_t includes a term for the drag force acting on the vegetation:

$$f_t = \tau_0 + Nf_d \tag{4}$$

where Nf_d is the drag force acting on the cylindrical obstacles in a control volume with a unit area, and f_d is the drag force on a cylindrical obstacle. Substituting the Manning roughness coefficient n in SI units and the drag coefficient C_D , we obtain

$$f_t = \frac{\rho g n^2 U^2}{h^{1/3}} + N C_D \frac{\rho U^2}{2} h d \tag{5}$$

For evaluations involving bed shear stress, we did not consider deformations of the vertical velocity profile, as in many two-dimensional analytical studies on rivers [16–20]. It is known that the vertical velocity profile varies between accelerating and decelerating flows [50] and with the resistance by the cylinder group [44]. In addition, because the presence of the cylinder group results in horseshoe vortices, a secondary resistance due to the cylinder

group, apart from the drag forces acting on them, is also generated [11]. To accurately evaluate the total resistance, an advanced model capable of calculating the non-equilibrium velocity profile [11] will be necessary. However, as indicated afterward, because the contribution of bottom shear stress to the total resistance is assumed to be much smaller than the drag force on the cylinders, the first term of Eq. (5) was simplified based on an assumption of a uniform velocity profile. When Eq. (5) is substituted into Eq. (3) for non-uniform flow, the water depth profile for a gradually varying flow with emergent vegetation can be obtained [38, 49]:

$$\frac{dh}{dx} = \frac{S_0 - \frac{n^2 U^2}{h^{4/3}} - \frac{C_D N d U^2}{2g}}{1 - \mathcal{F}^2} \tag{6}$$

The results for uniform flow ($dh/dx=0$) can then be deduced:

$$S_0 - \left(2 \frac{n^2}{h^{1/3}} + C_D N d h \right) \frac{U^2}{2gh} = 0 \tag{7}$$

For a flow that involves dense emergent vegetation, the drag coefficient term is known to be dominant over the bed friction term [26]. The bed friction term with $n=0.010$ estimated for the channel bed material (Styrofoam) used in this study is much smaller than the drag force terms (< 1% for Cases L1–L6 outlined in Table 1). In this study, the drag force acting on the emergent cylinders in the uniform open-channel flows (Cases L1–L6) was evaluated using Eq. (7), using averaged gradients of the total head $U^2/2g + h + z$, instead of S_0 , to minimize the effects of non-equilibrium flow.

4 Drag in uniform open-channel flows

In this study, the drag f_d , defined in Eq. (4), on an emergent obstacle in open-channel flows comprises three components: the base component f_0 , which excludes the effects of water surface variation and pressure gradients or drag forces acting on an infinitely long cylinder for deep uniform open-channel flows ($\mathcal{F}=0$); and two additional components f_s and f_p , associated with variations in the water surface and the pressure gradient attributed to the drag force, respectively.

$$f_d = f_0 + f_s + f_p \tag{8}$$

This section discusses f_s ; the other component f_p is discussed further in the paper in the section on the calculation of the water surface profile.

The base component f_0 has already been analyzed in several past studies. Typically, the drag force is composed of pressure and friction components, the former being dominant in flows with high Reynolds numbers [30, 32], in which the drag is attributed directly to the relative pressure Δp acting on an object in the flow. Herein, the relative pressure on a vertical cylinder is expressed as $\Delta p = p - p_0$, where p is the actual pressure acting on the cylinder surface, and p_0 is the pressure of the “free stream” or “undisturbed flow” [45–47] at that point without the objective cylinder. The pressure drag is often referred to as “form drag” because of its strong dependence on the shape or form of the object [30]. In general, pressure is described as a dimensionless pressure coefficient C_p based on the representative velocity U under free-stream or undisturbed-flow conditions as follows:

$$C_p = \frac{\Delta p}{\rho U^2 / 2} \quad (9)$$

Figure 4 shows the differential force for the base component of the drag force. For the free-stream condition without a water surface, the drag is calculated as

$$f_0 = \int_0^{2\pi} \Delta p \cos \theta dA \quad (10)$$

where $dA = h(d/2)d\theta$. By substituting Δp from Eq. (9) into Eq. (10), we obtain

$$f_0 = \frac{hd}{4} \rho U^2 \int_0^{2\pi} C_p \cos \theta d\theta \quad (11)$$

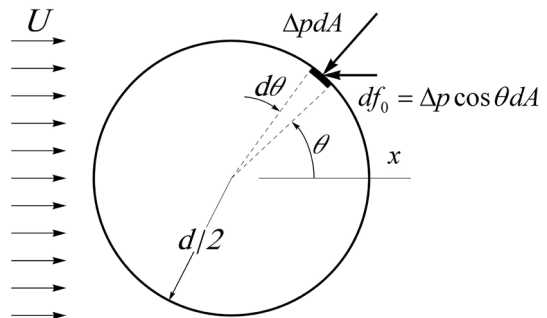
To obtain the drag coefficient for the base component, C_{D0} , we divide both sides of Eq. (11) by $0.5\rho U^2 hd$, yielding

$$C_{D0} = \frac{1}{2} \int_0^{2\pi} C_p \cos \theta d\theta \quad (12)$$

It should be noted from the projected area hd that the drag coefficient C_{D0} does not account for the water surface variation effect (i.e., the drag coefficient for a very small Froude number \mathcal{F}).

As the flow in an open channel passes around a cylinder, local water surface variations occur. The water surface profile around the cylinder is assumed to be superposed on an undisturbed open-channel flow, i.e., without the objective cylinder, and its variation Δh , as illustrated in Fig. 5. In this figure, the water level of the undisturbed open-channel flow for the objective cylinder is represented by a horizontal dashed line. Here, there is no pressure gradient in the streamwise direction of the undisturbed flow based on an assumption of a uniform flow. The additional term associated with the water surface variation, f_s in Eq. (8), is applied such that the other additional term is not considered (i.e., $f_p = 0$). The water surface variations Δh are induced by the pressure variation Δp around the cylinder under the water surface. Given that negative gauge pressures are untenable, the water level is reduced to the height of the zero-gauge pressure.

Fig. 4 Differential force acting on cylinder in free-stream flow for base component of drag force



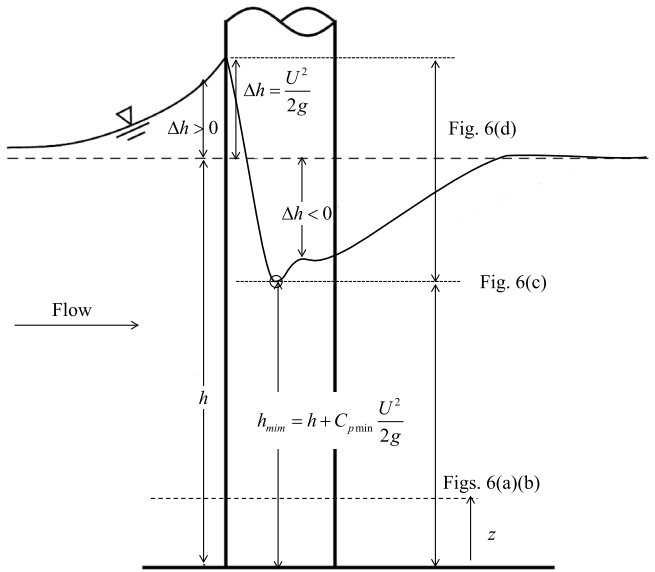


Fig. 5 Schematic of water surface profile around objective circular cylinder and definition of water surface variation Δh

To derive the effect of water surface variation around an emergent obstacle on the drag coefficient, we considered a typical pressure distribution around a cylindrical obstacle at an arbitrary water depth h (Fig. 6a). When the hydrostatic pressure in the undisturbed open-channel flow $\rho g(h - z)$ (where z is the height of the section) is subtracted from the actual pressure p , the result is Δp , distributed as shown in Fig. 6b. Based on an assumption of a constant Δp in the vertical direction and in the hydrostatic pressure distribution, $\Delta h(\theta)$ is defined as

$$\Delta h(\theta) = \frac{\Delta p(\theta)}{\rho g} = \frac{U^2}{2g} C_p(\theta) \tag{13}$$

where $C_p(\theta)$ is the pressure coefficient.

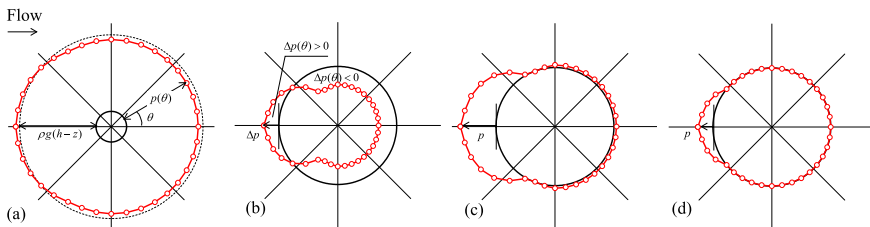


Fig. 6 Schematic figures of pressure distribution on objective cylinder at several heights defined in Fig. 5: **a** variation in pressure distribution, p , at depth $h - z$ below water surface at its normal level; **b** relative pressure distribution Δp ; **c** variation in pressure distribution at lowest water level of fluctuating part; **d** pressure distribution at a higher water level than in (c)

However, because of the range of variation in the water surface ($z > \Delta p_{\min}/\rho g$, Δp_{\min} : minimum value of the relative pressure Δp), the effect of the water surface needs to be considered in the relative pressure distribution. Figure 6c shows the pressure variation at $z = 0$ where $\Delta p = p$, whereas Fig. 6d shows an example between the highest water level (in front) and lowest water level. In this range, a zero-pressure value occurs above the water surface, and the distribution of the actual Δp values is different from that shown in Fig. 6b. This induces an additional force as an effect of the water surface variation in open-channel flow.

To formulate the problem, we focused on the water surface variation component of the drag f_s in Eq. (8). Based on sections at heights below the undisturbed water depth h , an additional pressure force Δf is required to compensate for negative pressures at angles with negative Δh , at which $\rho g(h - z) + \Delta p$ is negative. The additional differential force due to the water surface variation component, df_s , is defined as

$$df_s = \left(\frac{d}{2}d\theta\right)\frac{\rho g}{2}\Delta h^2 \tag{14}$$

Conversely, based on sections above the undisturbed water depth h , the same additional pressure as that appearing in Eq. (14) was applied under the assumption of a hydrostatic pressure distribution. Therefore, Eq. (14) is considered to be a definition of the infinitesimal force required to induce the water surface variation component of drag f_s for both negative and positive Δh , and the drag component f_s is given by

$$f_s = \int_0^{2\pi} \frac{\rho g d}{4} \Delta h^2 \cos \theta d\theta \tag{15}$$

Substituting Δh from Eq. (13) into Eq. (15), we obtain the water surface variation component of the drag, f_s :

$$f_s = \frac{\rho U^4}{16g} d \int_0^{2\pi} C_p^2 \cos \theta d\theta \tag{16}$$

Substituting Eqs. (11), (12), and (16) into Eq. (8) for uniform-flow conditions ($f_p = 0$), we obtain the following, using the drag coefficients C_D for f_d :

$$\frac{\rho U^2}{2} C_D h d = \frac{\rho U^2}{2} C_{D0} h d + \frac{\rho U^4}{16g} d \int_0^{2\pi} C_p^2 \cos \theta d\theta \tag{17}$$

Dividing both sides by $\rho U^2 C_{D0} h d / 2$ and substituting Eq. (12) into Eq. (17) yields the drag coefficient for open-channel flows.

$$\frac{C_D}{C_{D0}} = 1 + \frac{\beta_{Cp}}{2} C_{D0} \mathcal{F}^2 \tag{18}$$

The relative drag coefficient C_D/C_{D0} is proportional to the square of the Froude number, with the proportionality factor composed of C_{D0} and β_{Cp} . The coefficient β_{Cp} is defined as the second-order moment of the pressure coefficient around the cylinder, expressed as

$$\beta_{C_p} = \frac{\int_0^{2\pi} C_p^2 \cos \theta d\theta}{\left(\int_0^{2\pi} C_p \cos \theta d\theta \right)^2} \tag{19}$$

5 Experimental results for uniform flows

The drag coefficient for base component of the drag force, C_{D0} , and the coefficient β_{C_p} , calculated based on the distribution of the measured pressures on the cylinder, are listed in Table 2 and are compared with values calculated based on free stream-flow conditions [30]. Note that the coefficients β_{C_p} for accelerating flow that are outlined in Table 2 include the incremental drag due to the pressure gradient, which is described further in the paper, and are defined differently from the C_{D0} based on Eq. (8). Figure 7 shows the variations in C_{D0} and β_{C_p} with respect to vegetation density. Whereas the drag coefficient C_{D0} increases as the vegetation density increases, the coefficient β_{C_p} tends to decrease. This is because the pressure coefficient C_p used to determine β_{C_p} using Eq. (19) depends on the Reynolds number and the conditions of the cylinder array. Moreover, the symmetry between the variations in the drag coefficient C_{D0} and the variations in the coefficient β_{C_p} reveals a high correlation relationship between them. However, the available data are limited, and further study will be necessary to accurately predict the effect of water surface changes on the drag coefficient. Nonetheless, because all values of β_{C_p} calculated herein, as shown in Fig. 7, are negative, it can be inferred that the drag coefficient in an open-channel flow decreases as the Froude number increases, which is consistent with the findings of previous studies [34, 37].

Figure 8a shows the drag coefficient C_D as a function of the Froude number \mathcal{F} for the uniform-flow conditions listed in Table 1. Figure 8a enables comparisons between the experimental values in different hydraulic conditions and theoretical values based on Eq. (18). The drag-force coefficient based on the absence of water surface effects, or $\mathcal{F} \rightarrow 0$, i.e., C_{D0} , is necessary for Fig. 8. The value $C_{D0}=1.22$ is obtained to minimize the root-mean-square error (RMSE) between the measured drag coefficient and the drag

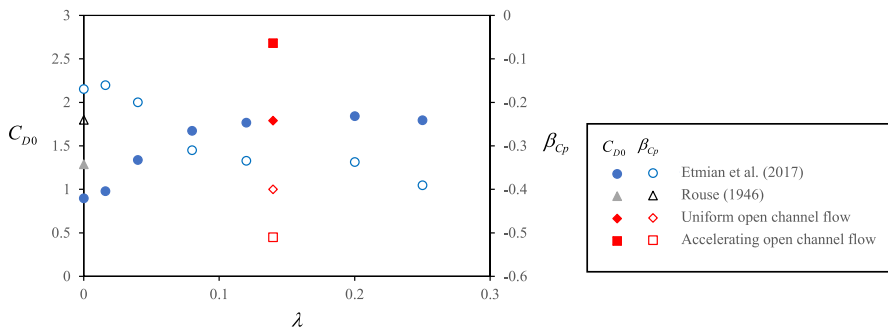


Fig. 7 Variations in the drag coefficient for the base component of drag force, C_{D0} , and coefficient β_{C_p} with respect to vegetation density λ for high Reynolds number, including data from Etmian et al. [44] for $\mathcal{R} = 1340$. Data for $\lambda = 0$ are for single cylinder

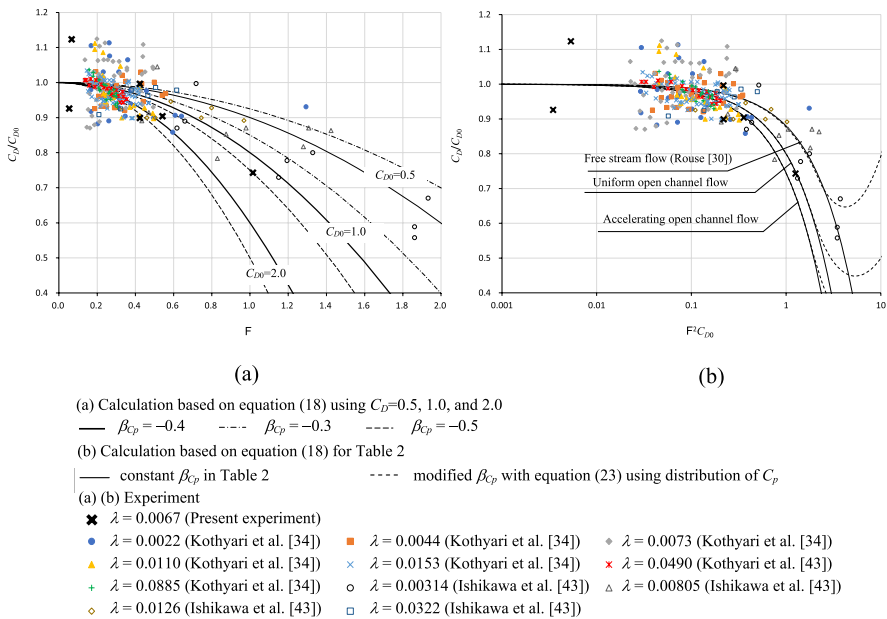


Fig. 8 C_D/C_{D0} as a function of Froude number: **a** effect of \mathcal{F} on experimental C_D data; **b** comparison between experimental data and theoretical results

coefficient calculated using Eq. (18), with the data subject to $\mathcal{F} < 0.5$. The value $C_{D0} = 1.79$ in Table 2 is a result of a three-cylinder row array with high velocity along the sidewall, whereas $C_{D0} = 1.22$ when a sufficient number of cylinders in a row are used in the experiment. However, the differences in C_{D0} can be explained by the blockage effect, because the C_{D0} values 1.22 and 1.79 become 0.76 and 0.81, respectively, after correction for the blockage effect, i.e., $C_D^*/C_{D0} = (1 - D/\Delta y)^{1.35}$ (C_D^* : corrected C_D for blockage effect) [51]. For comparison, Fig. 8 also includes previous experimental results from Kothyari et al. [34] and Ishikawa et al. [43] on emergent cylinders in uniform flows, in which the values of C_{D0} were obtained in the same manner as described previously, i.e., using Eq. (20). In line with the variations in C_{D0} and β_{Cp} shown in Fig. 7, the experimental data are compared with calculation results based on possible ranges of values of C_{D0} and β_{Cp} . Most of the experimental data are explained well within the range of the calculation results, except for a number of scattered values with low \mathcal{R} . This result demonstrated how the influence of the Froude number on the drag coefficient came to be overlooked. However, according to the relationship between C_D/C_{D0} and \mathcal{F} (Fig. 8a) for higher values of \mathcal{F} , the drag coefficient has an apparent tendency to decrease as the Froude number is increased, even in subcritical-flow conditions. This decrease in C_D/C_{D0} with respect to increasing \mathcal{F} was also confirmed when we compared the drag coefficients for Cases L3–L7 (as outlined in Table 1), in which \mathcal{F} varied within a small range of \mathcal{R} . The dependence of C_D on \mathcal{R} and \mathcal{F} is discussed as follows.

In Eq. (18), the drag coefficient C_D is used in conjunction with C_{D0} , β_{Cp} , and \mathcal{F} . The values of C_{D0} and β_{Cp} are defined by the pressure coefficient C_p , as expressed in Eqs. (12) and (19), respectively. Based on an assumption of a hydrostatic pressure distribution, as described earlier, C_p is supposed to be independent of \mathcal{F} , whereas C_D is a function of \mathcal{F}

and C_p . On the other hand, C_p around a cylinder can be expressed as a function of \mathcal{R} based on the similarity principle with respect to the Reynolds number for the Navier–Stokes equations [32]. From this, C_D can be considered a function of the two independent variables \mathcal{F} and \mathcal{R} , as $C_D(\mathcal{F}, \mathcal{R})$. The empirical Ergun formula has been applied to the calculation of drag coefficient on aligned cylinders [25, 26], as follows:

$$C_D = 2\left(\frac{\alpha_0}{\mathcal{R}} + \alpha_1\right) \tag{20}$$

Equation (20) represents the relationship between the drag coefficient and Reynolds number of a single body immersed in a free-stream flow with a relatively high Reynolds number [26]. The coefficients α_0 and α_1 of the equation have been investigated using experimental data and are known to be a function of the array characteristics.

If the C_{D0} in Eq. (18) is obtained using Eq. (20), and a constant β_{Cp} is assumed, the value of C_D can be expressed as a function of \mathcal{R} and \mathcal{F} as follows:

$$C_D = 2\left(\frac{\alpha_0}{\mathcal{R}} + \alpha_1\right) + \frac{\beta_{Cp}\mathcal{F}^2}{2} \left\{ 2\left(\frac{\alpha_0}{\mathcal{R}} + \alpha_1\right) \right\}^2 \tag{21}$$

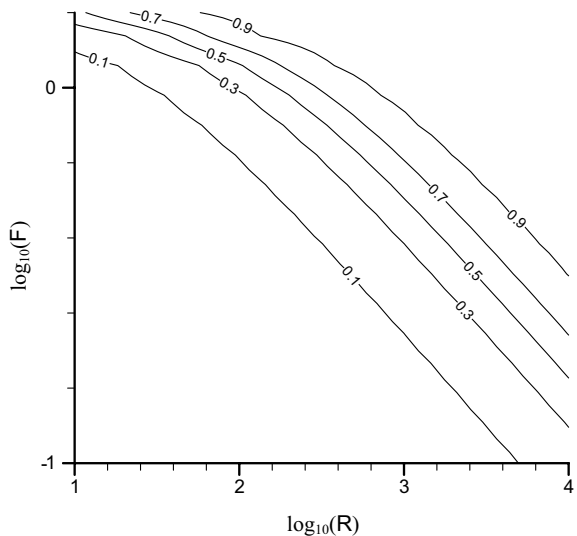
Calculating the total derivative of dC_D of Eq. (22) produces Eq. (23):

$$dC_D = \frac{\partial C_D}{\partial \mathcal{F}} d\mathcal{F} + \frac{\partial C_D}{\partial \mathcal{R}} d\mathcal{R} \tag{22}$$

$$\frac{dC_D}{C_{D0}} = -2\frac{\alpha_0}{C_{D0}\mathcal{R}} (1 + \beta_{Cp}C_{D0}\mathcal{F}^2) \frac{d\mathcal{R}}{\mathcal{R}} + \beta_{Cp}C_{D0}\mathcal{F}^2 \frac{d\mathcal{F}}{\mathcal{F}} \tag{23}$$

Referring to Tanino and Nepf [26] for the order of α_0 , we investigated the dependence of C_D on \mathcal{F} and \mathcal{R} for $C_{D0}=1$ and $\alpha_0=100$ (Fig. 9). Even in subcritical-flow conditions ($\log_{10}(\mathcal{F}) < 0$), the dependence of C_D on \mathcal{F} in flows with large Reynolds numbers is not

Fig. 9 Dependence of C_D on \mathcal{F} and \mathcal{R} for $C_{D0}=1$ and $\alpha_0=100$. Labels indicate values of $b/\sqrt{a^2 + b^2}$, where a, b are the coefficients of $d\mathcal{F}/\mathcal{R}, d\mathcal{F}/\mathcal{F}$, respectively, when Eq. (22) is rewritten as $dC_D/C_{D0} = a(d\mathcal{R}/\mathcal{R}) + b(d\mathcal{F}/\mathcal{F})$



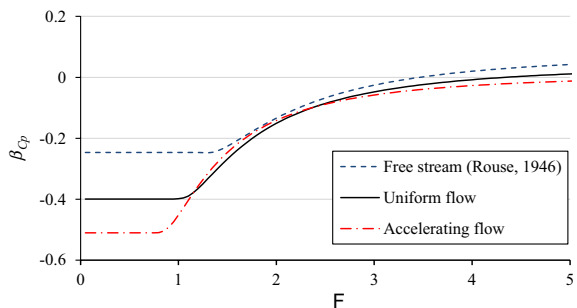
negligible relative to that on \mathcal{R} . For example, the effect of \mathcal{F} becomes apparent at approximately $\mathcal{F} = 0.3$ ($\log_{10}(\mathcal{F}) = 0.5$) for $\mathcal{R} = 10^3$.

In Fig. 8b, the theoretical lines calculated using Eq. (18) for free-stream, uniform, and accelerating open-channel flow conditions with constant values of β_{C_p} (Table 2) explain the decreasing trends exhibited by the experimental results. On the other hand, the decreasing trends exhibited by the experimental values of C_D/C_{D0} with respect to increasing $C_{D0}\mathcal{F}^2$ became milder compared to the theoretical decreasing trend based on Eq. (18) with constant values of β_{C_p} . Overall, the experimental results demonstrated a tendency to deviate from the theoretical lines at higher Froude numbers. In addition to the variation in β_{C_p} with hydraulic conditions, this result implies that, at high Froude numbers, Eq. (18) with constant β_{C_p} cannot be applied to very shallow-water-depth conditions behind the cylinder. The limitation of Eq. (18) is evident in the negative drag coefficients at high Froude numbers. Based on the uniform-flow condition $\beta_{C_p} = -0.4$, Eq. (18) cannot be applied to flows with $C_{D0}\mathcal{F}^2 > 5$ because the calculation produces a negative value for C_D . More specifically, for the constraint condition that satisfies the positive-water-depth condition $h + \Delta h > 0$, the limitation on Eq. (18) is derived from Eq. (13) using $C_{p\min}$, which takes the minimum water depth and value of C_p as $F^2 < -2/C_{p\min}$ ($C_{p\min} < 0$), based on an assumption of free-stream $C_p(\theta)$. For the condition $F^2 > -2/C_{p\min}$, the bed behind each cylinder was dried. Equation (13) for the Δh behind the cylinder must be modified to maintain the water depth at $h + \Delta h > 0$; thus, a penalty function is applied:

$$\Delta h = C'_p \frac{U^2}{2g}, \quad C'_p = \max\left(C_p, -\frac{2}{F^2}\right). \tag{24}$$

Equation (24) can be introduced to satisfy the constraint condition $h + \Delta h > 0$ for the calculation of β_{C_p} using Eq. (19), in conjunction with the measurement of the pressure coefficient distribution based on a uniform open-channel flow (Table 2). At high Froude numbers ($F^2 > -2/C_{p\min}$), the coefficient β_{C_p} must increase when the C'_p in Eq. (24) is used as the C_p in Eq. (19). For this uniform open-channel flow, the value of β_{C_p} increases from a constant value ($\beta_{C_p} = -0.24, -0.40, -0.51$) for the supercritical-flow condition, eventually becoming positive at high Froude numbers (Fig. 10), indicating that the drag force on the emergent object will increase at high Froude numbers. Based on the variation in the coefficient β_{C_p} , the theoretical values for the drag coefficients are modified, as indicated by the dashed lines in Fig. 8b. The relative drag coefficient C_D/C_{D0} attains its minimum value and gradually increases as the Froude number is increased. However, the theoretical lines based on Eq. (24) (dashed lines in Fig. 8) still underestimate the measured drag forces, which deviate from the solid theoretical lines over $C_{D0}\mathcal{F}^2 = 1$, where there is still little discrepancy

Fig. 10 Variation in coefficient β_{C_p} with Froude number \mathcal{F} using pressure coefficient distributions for free stream, uniform open-channel, and accelerating open-channel flows (outlined as conditions in Table 2) in conjunction with the constraint condition of Eq. (24)



between the solid and dashed lines. This discrepancy between the experimental results and the modified theoretical values is attributed to the occurrence of a vertical distribution of pressure change Δp induced by the vertical velocity distribution. By contrast, a uniform velocity distribution and a hydrostatic pressure distribution were assumed in the derivation of Eqs. (18) and (24) even for high Froude numbers. Because the velocity near the water surface is higher than the depth-averaged velocity, the actual effect of the water surface on the drag force is considered to be greater than that assumed in the present theory. Thus, the assumption that C_p is independent of \mathcal{F} , which was used to introduce Eqs. (18) and (21), is no longer satisfied at high \mathcal{F} conditions. However, although detailed investigations will be necessary for more accurate estimations of the drag coefficient, particularly for flows with high Froude numbers, Eq. (18) can be adopted as a first approximation of the drag coefficient in open-channel flows.

6 Calculation of water surface profile for flow with emergent cylinders

Before examining the validity of Eq. (18) for calculating water depth profiles in gradually varied flows in conjunction with Eq. (6), we examine the accuracy of the equations for the uniform subcritical flows (L1–L5), as visualized in Fig. 11.

Although the coefficient β_{Cp} varies with respect to the vegetation density, as indicated in Fig. 7, the coefficient is set to $\beta_{Cp} = -0.4$ in the upcoming analysis because the variation with respect to the density does not appear to be significant when the vegetation density is greater than 0.04. Furthermore, we want to focus on the effects of the non-equilibrium open-channel flows at the constant-density condition $\lambda=0.067$. The water surface profiles are calculated using Eq. (6) from the downstream end water depth at $x = -0.1$ m. The drag-force coefficient C_D is calculated with Eq. (18) for Run U1, whereas the constant $C_D=C_{D0}$ is applied for Run U2. The RMSEs between the results of the calculation and experiment for L3–L5 are larger than those for L1–L2, indicating that the RMSEs depend on the velocity head. For the calculations, $C_{D0}=1.22$ is adopted, which is obtained earlier in the study for Fig. 8. The RMSEs are affected by measurement errors and the uniform-velocity

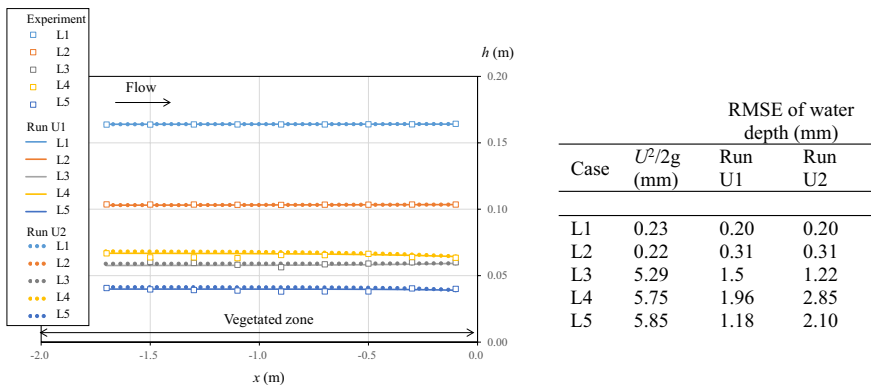


Fig. 11 Calculation results based on Eq. (6) and RMSEs of water depth for water surface profiles in uniform-flow conditions. Equation (18) with $C_{D0}=1.22$ is applied to Run U1, whereas constant $C_D=1.22$ is applied to Run U2. Symbols are measurement results; solid and dashed lines are calculated for Run U1 and U2, respectively

assumption introduced for Eq. (6). The velocity head causes the local water level to rise and is considered to be the representative length of the water surface measurement error, measured manually using a point gauge. The RMSEs are also affected by errors in the calculation model based on Eq. (6) from the momentum correlation coefficient in the advection term in Eq. (1) induced by the spatiotemporal variation in the velocity. The RMSEs of Run U1 are smaller than those of Run U2 except for Case L3, in which the effect of Eq. (18) for f_s on C_D is manifested in cases with relatively large \mathcal{F} . The experimental data and discussions in this paper regarding water depth are considered to include an order of error similar to the velocity head, i.e., a few millimeters at the maximum. The water surface profiles for L1–L5 are well reproduced within this scale.

Subsequently, the same calculation method with the same coefficients as those in Run U1 and U2 were applied to gradually varied flows, including accelerating and decelerating flows (Fig. 12). The calculation results from Eq. (6), in conjunction with Eq. (18) for C_D and constant $C_D=C_{D0}$, are indicated by dashed lines and small square symbols, respectively. Whereas the water depth profiles for the decelerating flows (b) were properly reproduced by the calculation results, those for the accelerating flows (a) were underestimated. Although the calculation method was designed to consider an error of a few millimeters even for uniform-flow conditions (Fig. 11), the underestimations by the calculations (Fig. 12a) were still significant relative to the error. On the other hand, compared to the differences between the measurement and calculation results of Eq. (6), the differences in the calculated results between Eq. (18) for C_D and constant $C_D=C_{D0}$ were negligible compared to the difference from the measured results because relatively high Froude number flow restricted to near the boundary. This indicates that accelerating flows involve a mechanism that increases the drag coefficient or resistance of the obstacles.

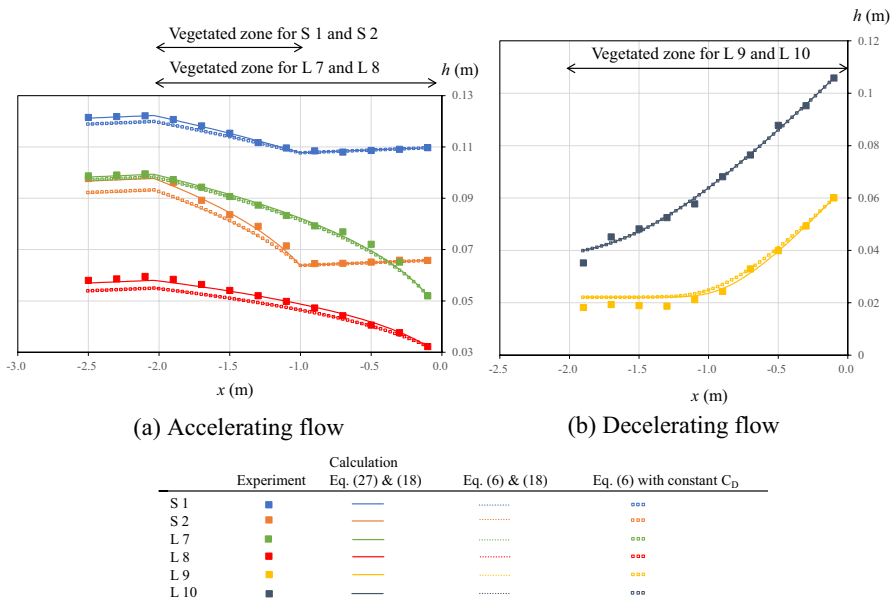


Fig. 12 Variation in water surface profile for gradually varied flows. Solid symbols are measurement results; solid lines are calculated using Eqs. (27) and (18); dashed lines are calculated using Eqs. (6) and (18) ($f=f_0+f_s$); no-fill, small square symbols are calculated using Eq. (6) with constant C_D ($f=f_0$)

As shown in Table 2, the pressure measurement around a cylinder also revealed that the base drag coefficient C_{D0} for the accelerating flow ($C_{D0}=2.68$) was larger than that for the uniform flow ($C_{D0}=1.79$). The base drag coefficients are calculated using the pressure coefficient C_p , which excludes the effect of the water surface from the coefficient, even though the coefficients β_{C_p} for accelerating flow include the effect of the pressure gradient, as mentioned in a previous section. Figure 13 compares the distributions of the pressure coefficients for a solitary cylinder in a free stream [30], and for a single cylinder in a cylinder group in uniform and accelerating open-channel flows. The C_p values of these experiments were calculated based on an assumption of $C_p=1$ at the stagnation point [44] to obtain an undisturbed water surface level, which is necessary for calculating the Δh distribution. Whereas the distributions of the positive pressure coefficients in front of the cylinder among the three cases are similar, the negative pressure coefficients in the separation zone differ. For the accelerating flow, the pressure in the separation zone decreases to values lower than those for the uniform flow, contributing to an increase in the drag coefficient for the accelerating flow. The mechanism whereby the pressure decreases in the separation zone is explained in Fig. 14, which compares the longitudinal water surface profiles for uniform and accelerating flows. It is assumed that, in the separation zone, the velocity is low [12, 39, 40], and the water depth is nearly constant; furthermore, there is exposure to the water depth just downstream from the separation zone. Therefore, the pressure in the separation zone is less for the accelerating flow than for the uniform flow because of the pressure gradient in the direction of flow.

The pressure reduction in the separation zone investigated in the experiment and visualized in Figs. 13 and 14 indicates that the additional drag force associated with the pressure gradient, f_p , in the accelerating flow should be considered in evaluating the drag force f_d of Eq. (8). The additional pressure due to the decrease in the separation area is expressed as

$$f_p = -\rho gh d L \frac{dh}{dx} \tag{25}$$

Fig. 13 Distributions of pressure coefficients around a solitary circular cylinder in free-stream flow (circles), and around a single cylinder in a group in uniform flow (squares) and accelerating flow (triangles)

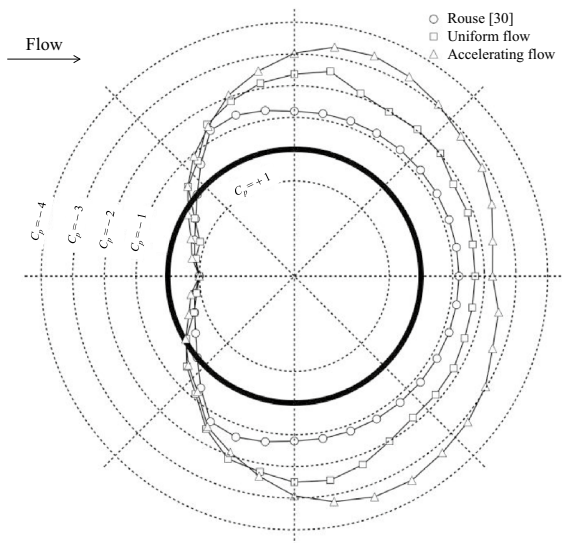
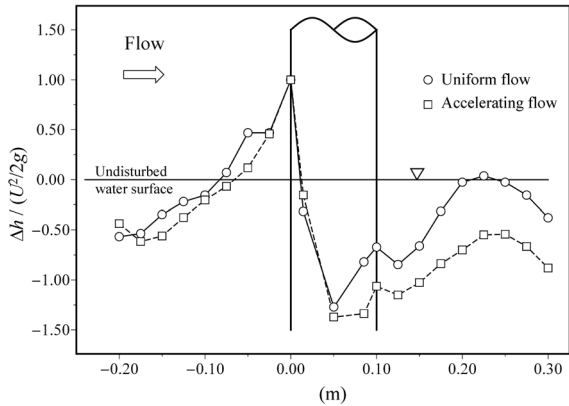


Fig. 14 Water surface profiles adjacent to circular cylinders in uniform and accelerating flows



where L is the representative length of the separation zone. Equation (25) is not attributed to the longitudinal buoyancy, which is calculated using $dL = \pi d^2/4$, but indicates an increasing form drag associated with a decrease in pressure in the separation zone for the negative pressure gradient. Based on an assumption that the representative length is expressed by the cylinder dowel diameter d as $L = kd$ (k , a coefficient), and a substitution of Eq. (25) into Eq. (8), the momentum equation for Eq. (1) can be re-written for steady flow conditions as follows:

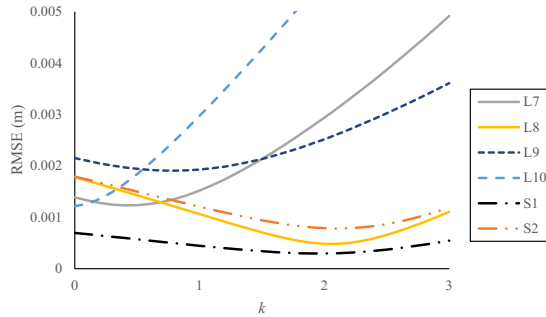
$$U \frac{dU}{dx} + g \frac{dh}{dx} = gS_0 - g \frac{n^2 U^2}{h^{4/3}} - N \left(C_D \frac{dU^2}{2} - gkd^2 \frac{dh}{dx} \right) \tag{26}$$

Equation (26) with a constant unit-width discharge (Eq. 2) yields the following depth profile equation for a flow with emergent vegetation:

$$\frac{dh}{dx} = \frac{S_0 - \frac{n^2 U^2}{h^{4/3}} - N \frac{C_D dU^2}{2g}}{1 - \mathcal{F}^2 - Nkd^2} \tag{27}$$

To calculate accelerating flows using Eq. (27), the coefficient k should be determined. In this study, the value k was obtained to minimize the discrepancies of water depth between the measurements and calculations based on Eq. (27).

Figure 15 shows the RMSEs of the calculation results at all measurement points against k for all accelerating and decelerating flows. For all cases, the RMSE decreases from $k=0$ and then increases after reaching a minimum, except for L10 in decelerating flow, which takes the minimum value at $k=0$. The k value yielding the minimum RMSE varied by case, ranging from 0.0 to 2.1. Therefore, for each case, the k value that yielded the minimum RMSE is applied to the calculation using Eq. (27). According to Fig. 15, the calculations based on Eq. (27) with appropriate values k yielded low RMSEs in all cases, and the minimized RMSEs, i.e., 0.29–1.23 mm, were not significant relative to those in uniform flows (Fig. 11). The water surface profiles calculated using Eq. (27) with appropriate k values from Fig. 15 were then compared with those based on the measurement results, as shown in Fig. 12. The results obtained using this calculation method are in good agreement with the measurement results. Although introducing Eq. (25), for the calculation of f_p , to the examination of decelerating flows had little effect on the validity of the analysis, the introduction of the additional drag force f_p from Eq. (8) into the examination of



Adjustment of parameter k to minimize RMSE of water depth for calculations based on Equation (27)

| | L7 | L8 | L9 | L10 | S1 | S2 |
|-----------|------|------|------|------|------|------|
| k | 0.4 | 2.1 | 0.8 | 0.0 | 1.9 | 2.1 |
| RMSE (mm) | 1.23 | 0.48 | 1.90 | 1.21 | 0.29 | 0.78 |

Fig. 15 Root-mean-square error (RMSE) of calculated water depths based on Eq. (27) as a function of coefficient k for the representative separation length

accelerating flows was demonstrated to be a necessity. It must be recalled that the calculations with Eq. (6), which adjusts the drag coefficient for the uniform flow and accounts for water surface effects with Eq. (18), could not reproduce the water depth profiles for non-uniform flows. Because the practical use of the numerical calculation of flows with obstacles necessitates evaluation of the drag force for non-uniform flows, it is significant that several non-uniform flows can be reproduced using a unified calculation method. It is known that the relative separation length to cylinder diameter varies depending on the hydraulic conditions, including the Reynolds number and obstacle arrangement condition [12, 39, 40], whereas the representative length introduced to evaluate the additional drag force in Eq. (25) is indirectly related to the separation length. On the other hand, with regard to the proper evaluation of L with the appropriate value of k , that remains a question for future research efforts to resolve.

7 Conclusions

This study proposed additional terms for the drag-force expression with the drag coefficient to include the effects of the water surface and the pressure gradient in an average scale. The effects of adding these terms were investigated through two types of laboratory experiments on uniform and non-uniform open-channel flows with emergent cylinders, focusing on the entire longitudinal water depth profile and the distribution of local pressure around the cylinder. The main results of the study are as follows:

- (1) Based on the assumption of hydrostatic pressure distribution, it was determined analytically that the drag coefficient C_D decreases in proportion to the square of the Froude number. The proportionality factor in the derived formula is composed of the drag coefficient of the base component of the drag force, C_{D0} , and the second-order moment of the pressure coefficient, β_{Cp} . The derived formula can reproduce the characteristics

of the drag force on emergent cylinders in a uniform flow, as obtained from our experiments and from others previously conducted.

- (2) For low Froude number flow, the water surface effects on the drag force for the depth profile calculation were negligible in this study. Although the drag coefficient formula for uniform flows can be applied to the calculation of water depth profiles in decelerating flows with emergent cylinders, the same formula led to an underestimation of resistance in accelerating flows, where the pressure in the separation zone decreased because of the negative gradient of the water depth in the longitudinal direction. Therefore, a modified method with additional drag-force terms accounting for the pressure drop in the separation zone was proposed. The accuracy of the acceleration flow reproduced therewith was improved considerably through the incorporation of this additional drag force into the calculation.

As reported in several past publications on the drag force in open-channel flows, the drag coefficient depends on hydraulic conditions and on several factors pertaining to the obstacles, such as their arrangements and shapes. Thus, estimating an appropriate value for the drag coefficient of the base component of the drag force is challenging. In fact, parameterization of the channel resistance coefficients is inevitably necessary in practical applications such as flood flow simulations of rivers [19, 20]. The most practical use of numerical calculations for flows with obstacles necessitates an evaluation of drag forces in non-uniform flows. The main contribution of this research is the development of an appropriate modification of the drag force from the base component for several non-uniform-flow conditions using a simple unified expression, which accounts for the open-channel effects due to water surface variation and pressure gradients in accelerating flows on the drag-force coefficient. It is expected to be particularly useful for resistance evaluation of obstacles in high Froude number flows with strong non-equilibrium and unsteadiness, such as dam-break flows and tsunamis, where both effects of the water surface and pressure gradient on the drag force are considered to be significant. In order to improve the validity of the analysis of the non-equilibrium flow field, it is necessary to clarify the effect of the pressure gradient on the drag force, i.e., the representative length L .

Acknowledgements The first author would like to acknowledge the support provided to this study through a JSPS KAKENHI grant (Number 18H01546).

Open Access This article is licensed under a Creative Commons Attribution 4.0 International License, which permits use, sharing, adaptation, distribution and reproduction in any medium or format, as long as you give appropriate credit to the original author(s) and the source, provide a link to the Creative Commons licence, and indicate if changes were made. The images or other third party material in this article are included in the article's Creative Commons licence, unless indicated otherwise in a credit line to the material. If material is not included in the article's Creative Commons licence and your intended use is not permitted by statutory regulation or exceeds the permitted use, you will need to obtain permission directly from the copyright holder. To view a copy of this licence, visit <http://creativecommons.org/licenses/by/4.0/>.


References

1. Kadlec RH (1990) Overland flow in wetlands: vegetation resistance. *J Hydraul Eng* 116(5):691–706. [https://doi.org/10.1061/\(ASCE\)0733-9429\(1990\)116:5\(691\)](https://doi.org/10.1061/(ASCE)0733-9429(1990)116:5(691))

2. Darby SE (1999) Effect of riparian vegetation on flow resistance and flood potential. *J Hydraul Eng* 125(5):443–454. [https://doi.org/10.1061/\(ASCE\)0733-9429\(1999\)125:5\(443\)](https://doi.org/10.1061/(ASCE)0733-9429(1999)125:5(443))
3. López F, García MH (2001) Mean flow and turbulence structure of open-channel flow through non-emergent vegetation. *J Hydraul Eng* 127(5):392–402. [https://doi.org/10.1061/\(ASCE\)0733-9429\(2001\)127:5\(392\)](https://doi.org/10.1061/(ASCE)0733-9429(2001)127:5(392))
4. Bennett SJ, Pirim T, Barkdoll BD (2002) Using simulated emergent vegetation to alter stream flow direction within a straight experimental channel. *Geomorphol* 44(1–2):115–126. [https://doi.org/10.1016/S0169-555X\(01\)00148-9](https://doi.org/10.1016/S0169-555X(01)00148-9)
5. Shaw RH, Schumann U (1992) Large-Eddy simulation of turbulent flow above and within a forest. *Boundary-Layer Meteorol* 61:47–64
6. Finnigan J (2000) Turbulence in plant canopies. *Annu Rev Fluid Mech* 32(1):519–571. <https://doi.org/10.1146/annurev.fluid.32.1.519>
7. Santiago JL, Coceal O, Martilli A, Belcher SE (2008) variation of the sectional drag coefficient of a group of buildings with packing density. *Boundary-Layer Meteorol* 128(3):445–457
8. Asher S, Niewerth S, Koll K, Shavit U (2016) Vertical variations of coral reef drag forces. *J Geophys Res Oceans* 121:3549–3563
9. Clifford NJ, Robert A, Richards KS (1992) Estimation of flow resistance in gravel-bedded rivers: a physical explanation of the multiplier of roughness length. *Earth Surface Process Landforms* 17(2):111–126
10. Nikora V, McLean S, Coleman S, Pokrajac D, McEwan I, Campbell L, Aberle J, Clunie D, Koll K (2007) Double-averaging concept for rough-bed open-channel and overland flows: applications. *J Hydraul Eng* 133(8):884–895
11. Uchida T, Fukuoka S, Papanicolaou AN, Tsakiris AG (2016) Nonhydrostatic quasi-3D model coupled with the dynamic rough wall law for simulating flow over a rough bed with submerged boulders. *J Hydraul Eng* 142(11):04016054. [https://doi.org/10.1061/\(ASCE\)HY.1943-7900.0001198](https://doi.org/10.1061/(ASCE)HY.1943-7900.0001198)
12. Ostanek JK, Thole KA (2012) Wake development in staggered short cylinder arrays within a channel. *Exp Fluids* 53:673–697. <https://doi.org/10.1007/s00348-012-1313-5>
13. Stoesser T, Kim SJ, Diplas P (2010) Turbulent flow through idealized emergent vegetation. *J Hydraul Eng* 136(12):1003–1017. [https://doi.org/10.1061/\(ASCE\)HY.1943-7900.0000153](https://doi.org/10.1061/(ASCE)HY.1943-7900.0000153)
14. Shimizu Y, Tsujimoto T (1992) Nakagawa H (1992) Numerical study on turbulent flow over rigid vegetation-covered bed in open channels. *Doboku Gakkai Ronbunshu* 447:35–44. https://doi.org/10.2208/jsej.1992.447_35
15. Nikora V, McEwan I, McLean S, Coleman S, Pokrajac D, Walters R (2007) Double-averaging concept for rough-bed open-channel and overland flows: theoretical background. *J Hydraul Eng* 133(8):873–883. [https://doi.org/10.1061/\(ASCE\)0733-9429\(2007\)133:8\(873\)](https://doi.org/10.1061/(ASCE)0733-9429(2007)133:8(873))
16. Zhang M, Li CW, Shen Y (2013) Depth-averaged modeling of free surface flows in open channels with emerged and submerged vegetation. *Appl Math Modell* 37(1):540–553
17. Nadaoka K, Yagi H (1998) Shallow-water turbulence modeling and horizontal large-eddy computation of river flow. *J Hydraul Eng* 124(5):493–500
18. Wu (2007) Computational river dynamics, Chapter 10, pp 375–402. Taylor & Francis, UK
19. Uchida T, Fukuoka S, Ishikawa T (2014) 2D numerical computation for flood flow in upper river basin with tributary inflows by using water level hydrographs observed at the main stream. *J Flood Risk Manag* 7(1):81–88. <https://doi.org/10.1111/jfr3.12019>
20. Shimizu R, Uchida T, Kawahara Y (2021) Flood analysis in the Nuta River basin during the heavy rain in July 2018. *J JSCE* 9(1):221–229. https://doi.org/10.2208/journalofjsce.9.1_221
21. Patel VC (1998) Perspective (1998): Flow at high Reynolds number and over rough surface-Achilles heel of CFD. *J Fluid Eng* 120(3):434–444
22. Kim SJ, Stoesser T (2011) Closure modeling and direct simulation of vegetation drag in flow through emergent vegetation. *Water Resour Res* 47(10):W10511. <https://doi.org/10.1029/2011WR010561>
23. Nepf HM (1999) Drag, turbulence, and diffusion in flow through emergent vegetation. *Water Resour Res* 35(2):479–489. <https://doi.org/10.1029/1998WR900069>
24. White BL, Nepf HM (2003) Scalar transport in random cylinder arrays at moderate Reynolds number. *J Fluid Mech* 487:43–79. <https://doi.org/10.1017/S0022112003004579>
25. Koch DL, Ladd AJC (1997) Moderate Reynolds number flows through periodic and random arrays of aligned cylinders. *J Fluid Mech* 349:31–66. <https://doi.org/10.1017/S002211209700671X>
26. Tanino Y, Nepf HM (2008) Laboratory investigation of mean drag in a random array of rigid, emergent cylinders. *J Hydraul Eng* 134(1):34–41. [https://doi.org/10.1061/\(ASCE\)0733-9429\(2008\)134:1\(34\)](https://doi.org/10.1061/(ASCE)0733-9429(2008)134:1(34))
27. Tinoco RO, Cowen EA (2013) The direct and indirect measurement of boundary stress and drag on individual and complex arrays of elements. *Exp Fluids* 54:1509. <https://doi.org/10.1007/s00348-013-1509-3>

28. Sonnenwald F, Hart JR, West P, Stovin VR, Guymer I (2017) Transverse and longitudinal mixing in real emergent vegetation at low velocities. *Water Resour Res* 53(1):961–978. <https://doi.org/10.1002/2016WR019937>
29. Sonnenwald F, Stovin V, Guymer I (2019) Estimating drag coefficient for arrays of rigid cylinders representing emergent vegetation. *J Hydraulic Res* 57(4):591–597. <https://doi.org/10.1080/00221686.2018.1494050>
30. Rouse H (1946) *Elementary mechanics of fluids* p.239(Fig.122). Dover, New York.
31. Naudascher E (1991) Hydrodynamic forces, IAHR hydraulic structures design manual 3. A. A. Balkema, Rotterdam/Brookfield.
32. Schlichting H, Gersten K (2000) *Boundary-layer theory*, 8th edn. Springer, Berlin. <https://doi.org/10.1007/978-3-642-85829-1>
33. Ergun S (1952) Fluid flow through packed columns. *Chem Eng Prog* 48(2):89–94
34. Kothiyari UC, Hayashi K, Hashimoto H (2009) Drag coefficient of unsubmerged rigid vegetation stems in open channel flows. *J Hydraul Res* 47(6):691–699. <https://doi.org/10.3826/jhr.2009.3283>
35. Cheng NS (2013) Calculation of drag coefficient for arrays of emergent circular cylinders with pseudo-fluid model. *J Hydraul Eng* 139(6):602–611. [https://doi.org/10.1061/\(ASCE\)HY.1943-7900.0000722](https://doi.org/10.1061/(ASCE)HY.1943-7900.0000722)
36. Cheng NS (1997) Effect of concentration on settling velocity of sediment particles. *J Hydraul Eng* 123(8):728–731. [https://doi.org/10.1061/\(ASCE\)0733-9429\(1997\)123:8\(728\)](https://doi.org/10.1061/(ASCE)0733-9429(1997)123:8(728))
37. Huai WX, Wu ZL, Qian ZD, Geng C (2011) Large eddy simulation of open channel flows with non-submerged vegetation. *J Hydrodyn* 23(2):258–264. [https://doi.org/10.1016/S1001-6058\(10\)60111-4](https://doi.org/10.1016/S1001-6058(10)60111-4)
38. Busari AO, Li CW (2016) Bulk drag of a regular array of emergent blade-type vegetation stems under gradually varied flow. *J Hydro-Enviro Res* 12:59–69. <https://doi.org/10.1016/j.jher.2016.02.003>
39. Braza M, Perrin R, Hoarau Y (2006) Turbulence properties in the cylinder wake at high Reynolds numbers. *J Fluids Struct* 22(6):757–771
40. Norberg C (1998) LDV-measurements in the near wake of a circular cylinder, ASME Paper No. FEDSM98–521:41–45.
41. Hayashi K, Fujii M, Shigemura T (2001) Fluid forces acting on multiple flows of circular cylinders in open-channel flow. *Ann J Hydraul Eng JSCE* 45:475–480 ((in Japanese))
42. Wu F-C, Shen HW, Chou Y-J (1999) Variation of roughness coefficients for unsubmerged and submerged vegetation. *J Hydraul Eng* 125(9):934–942
43. Ishikawa Y, Mizuhara K, Ashida M (2000) Drag force on multiple rows of cylinders in an open channel, grant-in-aid research project Report no. 10555176, H. Hashimoto, Kyushu University, Fukuoka, Japan [in Japanese].
44. Etmian V, Lowe RJ, Ghisalberti M (2017) A new model for predicting the drag exerted by vegetation canopies. *Water Resour Res* 53(4):3179–3196
45. Akiki G, Moore WC, Balachandar S (2017) Pairwise-interaction extended point-particle model for particle-laden flows. *J Comput Phys* 351:329–357
46. Balachandar S (2020) Lagrangian and Eulerian drag models that are consistent between Euler-Lagrange and Euler-Euler (two-Fluid) approaches for homogeneous systems. *Phys Rev Fluids* 5:084302
47. Yokojima S, Uchida T, Kazehaya Y, Kawahara Y: Undisturbed fluid flow for improved macroscopic estimation of drag forces acting on circular cylinders. In: Proceedings of 22nd congress of the international association for hydro-environment engineering and research-Asia Pacific Division, IAHR-APD 2020: Creating Resilience to Water-Related Challenges.
48. Cheng NS, Nguyen HT (2011) Hydraulic radius for evaluating resistance induced by simulated emergent vegetation in open-channel flows. *J Hydraul Eng* 137(9):995–1004. [https://doi.org/10.1061/\(ASCE\)HY.1943-7900.0000377](https://doi.org/10.1061/(ASCE)HY.1943-7900.0000377)
49. Chow VT (1959) *Open-channel hydraulics*. McGraw-Hill, New York. <https://doi.org/10.1016/j.jcp.2017.07.056>
50. Song T, Graf WH (1994) Non-uniform open-channel flow over a rough bed. *J Hydrosoci Hydraul Eng* 12(1):1–25
51. Ranga Raju KG, Rana OPS, Asawa GL, Pillai ASN (1983) Rational assessment of blockage effect in channel flow past smooth circular cylinders. *J Hydraul Res* 21(4):289–302. <https://doi.org/10.1080/00221688309499435>

Authors and Affiliations

Tatsuhiko Uchida¹  · Toshiki Ato² · Daisuke Kobayashi³ · Mahmoud F. Maghrebi⁴ · Yoshihisa Kawahara⁵

Toshiki Ato
ato.toshiki@cals-hokkaido.net

Daisuke Kobayashi
d202383@hiroshima-u.ac.jp

Mahmoud F. Maghrebi
maghrebi@um.ac.ir

Yoshihisa Kawahara
kawahr@hiroshima-u.ac.jp

- ¹ Graduate School of Advanced Science and Engineering, Hiroshima University, 1-4-1 Kagamiyama, Higashi-Hiroshima City, Hiroshima 739-8527, Japan
- ² Hokkaido Government, Kita 3-jo, Nishi 6-chome, Chuo-ku, Sapporo 060-8588, Japan
- ³ Graduate School of Engineering, Hiroshima University, 1-4-1 Kagamiyama, Higashi-Hiroshima City, Hiroshima 739-8527, Japan
- ⁴ Civil Engineering Department, Ferdowsi University of Mashhad, Azadi Sq, Mashhad, Iran
- ⁵ Office of Academic Research and Industry-Academia-Government and Community Collaboration, Hiroshima University, 1-4-1 Kagamiyama, Higashi-Hiroshima City, Hiroshima 739-8527, Japan